Texture and Microstructure Analysis of IN718 Nickel Superalloy Samples Additively Manufactured by Selective Laser Melting

Benjamin de Jager, Baicheng Zhang, Xu Song, Chryssanthi Papadaki, Hongjia Zhang, León Romano Brandt, Enrico Salvati, Tan Sui and Alexander M. Korsunsky*, *Member, IAENG*

Abstract — **Selective Laser Melting (SLM) is an additive manufacturing technique in which thin layers of fine powder are fused by selective melting with a high-powered laser to create a 3D product from a computer file. The high cooling rate of the melt pool formed by the high-powered laser gives rise to material microstructures that differ from standard wrought or cast material. Electron Backscattered Diffraction (EBSD) was performed on five IN718 samples with the long axis inclined with respect to the base plane by the different angles of 0°, 30°, 45°, 60°, and 90°, respectively. On the basis of the data collected, using the Orientation Distribution Function (ODF) and anisotropic elastic constants for the alloy, Young's modulus estimates for the five samples were obtained. Young's modulus appears to attain the highest value for the build orientation close to 45°. Fourier coefficients of each sample's ODF were analysed. It was found that the samples could be clearly distinguished by considering the fourth-order term.**

***Index Terms*—EBSD, Microstructure, Ni Superalloys, Selective Laser Melting**

Manuscript received Feb 06, 2017.

This work was supported in part by EU FP7 project iSTRESS ''Pre-standardisation of incremental FIB micro-milling for intrinsic stress evaluation at the sub-micron scale", and by EPSRC (UK) through grants EP/I020691 "Multi-disciplinary Centre for In-situ Processing Studies (CIPS)", EP/G004676 "Micromechanical Modelling and Experimentation", EP/H003215 "New Dimensions of Engineering Science at Large Facilities". Support from SIMTech is acknowledged through SIMT/14-230003, Selective Laser Melting (WP2), and SIMT/16-230001, Development of Hybrid 3D Additive + Subtractive Manufacturing Equipment (WP4).

Benjamin de Jager is with the Department of Engineering Science, University of Oxford, OX1 3PJ, UK (e-mail: ben@dejager.uk.com).

Baicheng Zhang is Scientist with the A*STAR Singapore Institute of Manufacturing Technology (SIMTech), 20 Biopolis Way, #08-01 Centros Building, Singapore 138668 (zhangbc@SIMTech.a-star.edu.sg).

Xu Song Scientist III with the A*STAR Singapore Institute of Manufacturing Technology (SIMTech), 20 Biopolis Way, #08-01 Centros Building, Singapore 138668 (xsong@SIMTech.a-star.edu.sg).

Chryssanthi Papadaki is doctoral student in the Department of Engineering Science, University of Oxford, OX1 3PJ, UK (e-mail: chrysanthi.papadaki@eng.ox.ac.uk).

Hongjia Zhang, is doctoral student in the Department of Engineering Science, University of Oxford, OX1 3PJ, UK (e-mail: hongjia.zhang@eng.ox.ac.uk).

León Romano Brandt is doctoral student in the Department of Engineering Science, University of Oxford, OX1 3PJ, UK (e-mail: leon.romanobrandt@eng.ox.ac.uk).

Enrico Salvati is doctoral student in the Department of Engineering Science, University of Oxford, OX1 3PJ, UK (e-mail: enrico.salvati@eng.ox.ac.uk).

Tan Sui is postdoctoral researcher in the Department of Engineering Science, University of Oxford, OX1 3PJ, UK (e-mail: tan.sui@eng.ox.ac.uk).

*Alexander M. Korsunsky is Professor of Engineering Science at the University of Oxford, OX1 3PJ, UK (corresponding author, tel: +44-18652-73043; fax: +44-18652-73010; e-mail: alexander.korsunsky@eng.ox.ac.uk).

I. Introduction

Additive manufacturing (AM) in metals is a process used to create three-dimensional parts from a digital file, and involves building up thin layers of material to create complete parts, often in complex shapes that are difficult to produce via casting, forging or machining. Several AM techniques have been proposed; some use wire as initial material (e.g. shaped metal disposition) whereas others use metallic powders (e.g. selective laser melting (SLM) and selective laser sintering (SLS)). With SLM, thin layers of atomized fine powder are fused by selectively melting the powder with a high-powered laser beam to form 2D slices of the 3D end product; this process is repeated layer by layer until the end product is complete.

The layer-by-layer process and high cooling rate of the small melt pool in SLM causes material microstructures different to standard wrought or cast material, affecting grain elongation and orientation. The aim of this study is to determine the effect of sample build orientation on microstructure of SLM Ni superalloys.

II. Materials and Methods

A. Materials

Inconel 718 (IN718), a precipitation hardenable nickel-chromium-based superalloy, in powder form was used to produce a set of dogbones by SLM with the orientation angles between the growth direction and the base plane ranging from 0° to 90°, at 15° intervals. A global system of axes (*ND*, *RD*, *TD*) was defined with respect to the base plate as illustrated in Figure 1, so that *ND* corresponds to the sample growth direction, and *TD* and *RD* are two in-plane directions with respect to which the laser beam path is defined in each layer. In addition, for each sample a local reference frame was also defined, with the longitudinal direction (*L*) corresponding to greatest extent of each dogbone sample, and the transverse direction (*T*) and the short transverse direction (*ST*) corresponding to the rectangular cross-section's larger and smaller dimensions, respectively.

Coupons were extracted from the dogbone samples with the 0°, 30°, 45°, 60° and 90° orientation angles with respect to the base plane, and used to determine the effect of build orientation on the microstructure (grain morphology and crystal lattice orientation, i.e. texture). For each sample,

ISBN: 978-988-14047-7-0
ISSN: 2078-0958 (Print); ISSN: 2078-0966 (Online)

EBSD analysis was performed on the three faces with the normals in the *L*, *T* and *ST* directions, respectively. By combining the microstructure maps obtained from each face, a pseudo-3D reconstruction of the sample microstructure 'cube' was obtained. Based on the data collected, Orientation Distribution Function (ODF) for the samples was evaluated using MTEX toolbox [1], and overall stiffness (effective Young's modulus) in the longitudinal direction was estimated.

B. Preparation Methods

Samples were prepared using standard metallographic procedures, with the final polish applied using 0.04μm colloidal silica. Scanning electron microscopy (SEM) and electron backscattered diffraction (EBSD) were performed using TESCAN LYRA3 FIB-SEM fitted with Oxford Instruments NordlysNano EBSD system at the Multi-Beam Laboratory for Engineering Microscopy (MBLEM), Oxford. Beam voltage of 10kV was used for analysis, and an EBSD map size of 300μm×300μm with a step size of 2.5μm was acquired for each face.

III. Results

A. Surface Microstructure

EBSD was used to determine the grain size distribution and the crystallographic texture of SLM-built samples, and MTEX toolbox for Matlab® was used to interpret the EBSD data.

Figure 2 shows pseudo-3D reconstructions for each of the five samples analysed (0°, 30°, 45°, 60° and 90°), coloured to represent the lattice orientation at each probe point using the basic crystallographic triangle for cubic material, according to the legend shown in Figure 2. Euler angles φ_1, Φ, φ_2 of individual faces were rotated so that the maps for all faces refer to the common consistent orientation with respect to the global axis *ND*, *RD*, *TD*.

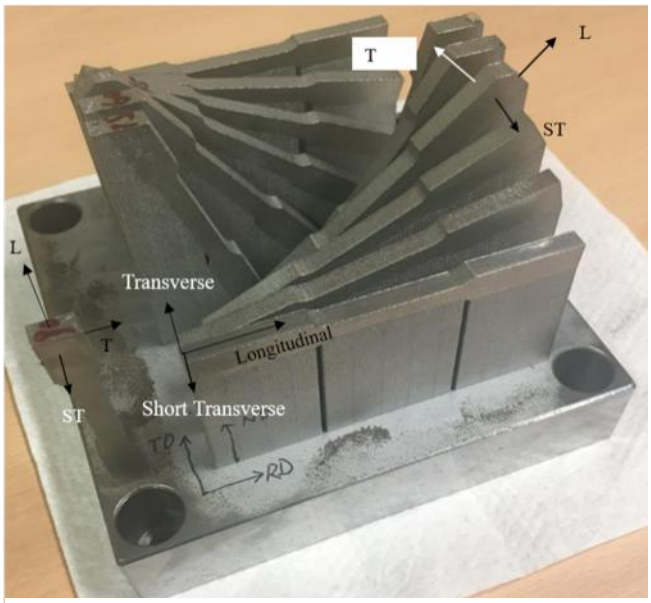

Figure 1: The family of SLM Ni dogbone samples of different orientation with respect to the base plane, as indicated by the labels. The lab frame axes are defined with respect to the base plate, and the local reference frame (*L*,*T*,*ST*) is shown for the 45° dogbone sample as an example.

Since EBSD mapping only encompasses a 300μm×300μm area for each face, it provides a limited sampling representation of the grain structure and orientation. In comparison, techniques such as X-ray diffraction allow sampling larger volumes and may provide improved statistics compared to the present study.

Table 1: Mean grain diameter, aspect ratio and grain inclination angle for the *L*, *T* and *ST* faces of all samples.

0°	**d** *(μm)*	**Aspect ratio** *(r)*	**Inclination angle** *(°)*
L	24.14	4.03	-1.28
T	16.17	2.01	5.34
ST	27.46	3.33	0.77
30°	**d** *(μm)*	**Aspect ratio** *(r)*	**Inclination angle** *(°)*
L	18.45	2.62	-2.05
T	18.35	2.18	-1.63
ST	27.48	3.98	25.88
45°	**d** *(μm)*	**Aspect ratio** *(r)*	**Inclination angle** *(°)*
L	19.36	2.37	4.48
T	19.60	2.22	-4.89
ST	25.40	4.08	39.20
60°	**d** *(μm)*	**Aspect ratio** *(r)*	**Inclination angle** *(°)*
L	17.22	2.18	37.16
T	21.04	2.53	6.07
ST	23.61	4.41	62.25
90°	**d** *(μm)*	**Aspect ratio** *(r)*	**Inclination angle** *(°)*
L	16.03	2.25	-14.39
T	27.20	5.39	-1.22
ST	19.83	3.90	2.12

Figure 3 shows plots of the grain inclination angle for the three faces with mutually orthogonal normal for the five samples.

The 0° sample shows a high degree of equiaxing on the *T* face, with a mean grain diameter of 16.17μm, which is lower than that of either of the *L* and *ST* faces (24.14μm and 27.46μm respectively). Figure 3 shows that the inclination angle distribution on the T face is roughly uniform across the [-90, 90] angle range, whereas the grains on the *L* and *ST* faces have a peak in the distribution at roughly zero degrees, with average angle 1.15° and -2.32°, indicating elongation in the *T* direction (growth direction).

The 30° sample shows grains on the *ST* face oriented and elongated along the growth direction, at 30° to the axis of symmetry of the face. The effects of build angle are predominantly visible on this face rather than the other two; this is because any grain elongation along the growth direction is normal to this face, allowing it to be seen clearly. By contrast, any elongation along the *L* and *T* directions will be seen as a projection onto the surface and thus less clearly visible via EBSD. Both the other two faces are largely equiaxed, and the histogram of inclination angle shows a roughly uniform distribution. Notable is the fact that the colouration of the *T* face has less red than the corresponding face on the 0° sample, which is to be expected since the growth direction is no longer parallel to the (001) local crystal axis.

ISBN: 978-988-14047-7-0
ISSN: 2078-0958 (Print); ISSN: 2078-0966 (Online)

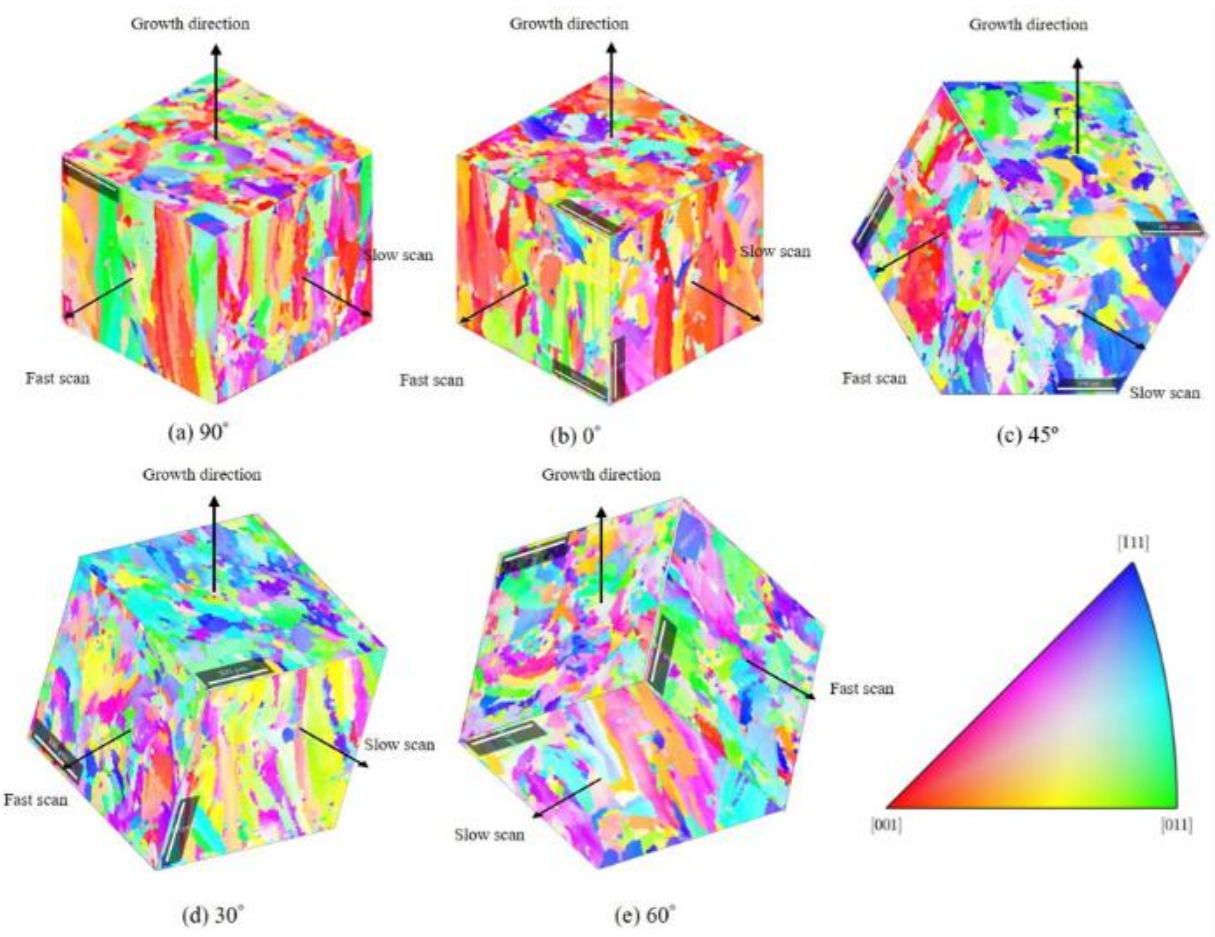

Figure 2: Pseudo-3D reconstructions of the EBSD maps for each sample with consistent colourisation according to the basic crystallographic triangle

The 45° sample has growth direction at 45° to all three faces; as with the 30° sample, the *ST* face is of particular interest. The *ST* face is observed to have mean grain inclination angle at 39.20° with a similar diameter to the *ST* face on the 0° sample (25.40µm vs 27.46µm), indicating grain elongation along the growth direction. Both the *T* and *L* faces have growth direction at 45° to their normal vectors, and correspondingly display similar grain diameters (19.60µm and 19.36µm respectively). The inclination distribution histograms for the *T* and *L* faces show small peaks around 90° and -90°, indicating that there is a degree of orientation along the projection of the growth direction onto these faces.

The 60° sample displays many similar characteristics to the 30° sample; the *ST* face is observed to have mean grain inclination angle of 62.25°, indicating elongation along the growth direction. Again, the colouration of the *L* and *T* faces shows the effect of the build angle on crystal orientation, which is at 60° to the local (001) crystal axis. The *T* face has a higher degree of grain elongation compared to the *L* face, shown by the aspect ratios of *X* and *Y* respectively, which is expected since the projection of the 60° angle onto the *T* face is more visible than on the *L* face.

The 90° sample has the same geometry as the 0° sample; however, the *L*, *T* and *ST* directions are rotated by 90° such that the growth direction is now along *L* rather than *T*. Grains on the *T* and *ST* faces have a larger diameter and an inclination angle close to 0° (-1.22° and 2.12° respectively) demonstrating elongation along the sample growth direction. The *ND* face has finer grains which are more equiaxed, indicating a stronger basal texture. In Figure 3 it can be seen that the peak of the *T* and *ST* distributions is around 0^o with fewer than 10% of grains having an inclination angle of more than ±20°.

B. Stiffness

In addition to the reconstruction and analysis of EBSD data, MTEX toolbox also allows carrying out the analysis of sample stiffness. The MTEX functionality outputs the Voigt, Reuss and Hill average stiffness tensors, which are computed from the single crystal elastic stiffness coefficients and the knowledge of the sample ODF. Below, the stiffness matrix for a cubic crystal is listed, along with the corresponding elastic coefficients for nickel superalloy possessing cubic crystal symmetry (fcc lattice) in Table 2.

The stiffness matrix for a crystal with cubic symmetry has the form (in the Voigt notation):

$$\mathbf{C} = \begin{bmatrix} C_{11} & C_{12} & C_{12} & 0 & 0 & 0 \\ C_{12} & C_{11} & C_{12} & 0 & 0 & 0 \\ C_{12} & C_{12} & C_{11} & 0 & 0 & 0 \\ 0 & 0 & 0 & C_{44} & 0 & 0 \\ 0 & 0 & 0 & 0 & C_{44} & 0 \\ 0 & 0 & 0 & 0 & 0 & C_{44} \end{bmatrix}$$

ISBN: 978-988-14047-7-0
ISSN: 2078-0958 (Print); ISSN: 2078-0966 (Online)

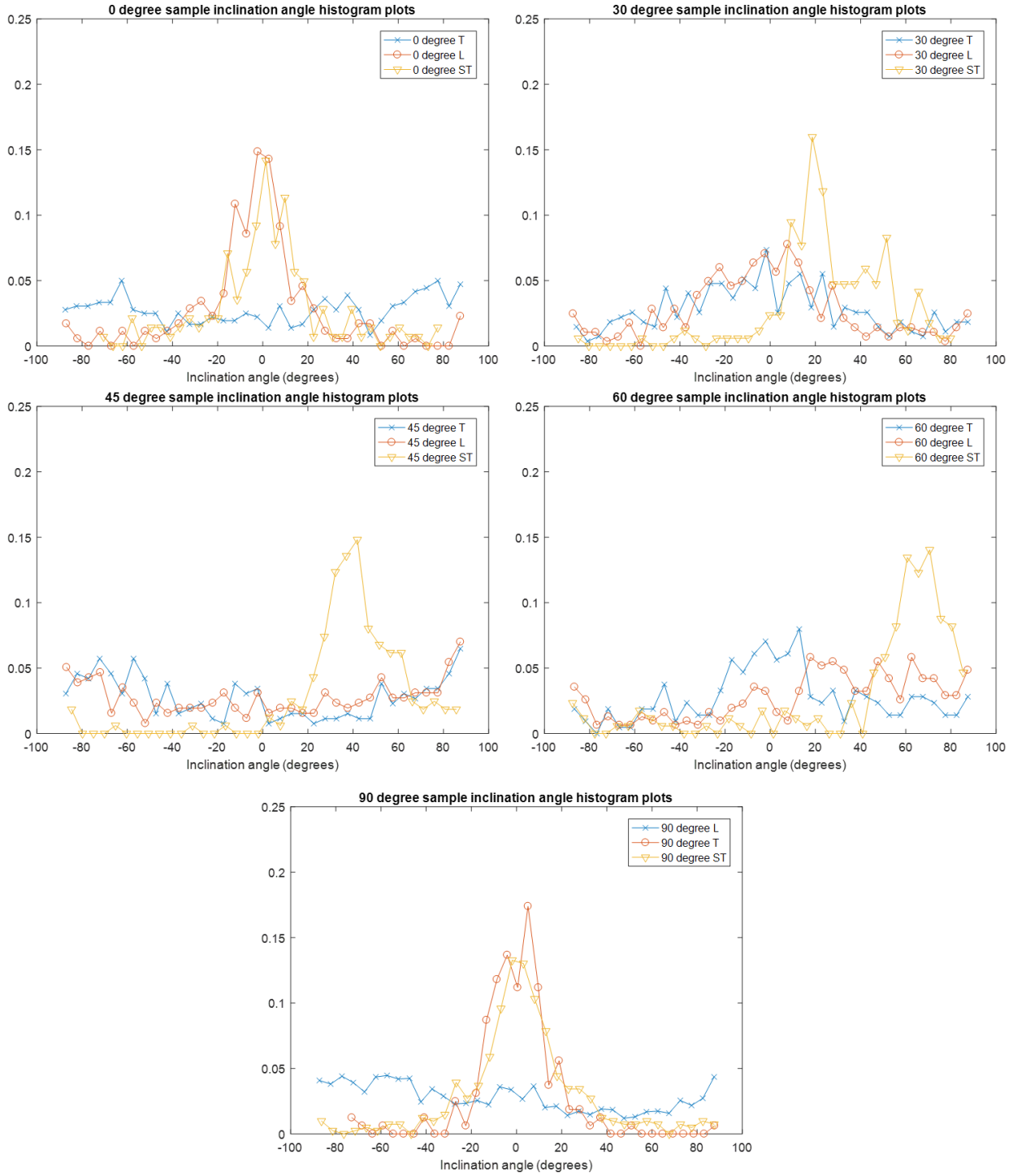

Figure 3: Histogram plots showing the inclination angle distribution for all three sides of all five samples

Table 2: Elastic stiffness coefficients for the fcc nickel superalloy IN718 [2]

Material	C_{11} $(10^{11}\ N/m^2)$	C_{12} $(10^{11}\ N/m^2)$	C_{44} $(10^{11}\ N/m^2)$
Nickel	2.508	1.500	1.235

The stiffness matrix of a single crystal gives the values of the elastic coefficients with respect to the system of coordinates associated with the crystal axes, i.e. aligned with the edges of the cubic unit cell. For crystals of any other orientation described by the three Euler angles, the corresponding stiffness matrix needs to be obtained using correct transformation which arises as a consequence of the contracted Voigt notation (6-vector notation) for stresses and strains that is implied in the above 6×6 form of the stiffness matrix [2].

The average orientation distribution function (ODF) was calculated from the entire set of EBSD data for each sample. From this, it was possible to calculate the average material tensors, which were used to calculate the longitudinal Young's modulus values for all samples using both Voigt and Reuss averaging. It is worth noting that EBSD analysis only provides data about the exterior grains for each sample, so an implicit assumption has to be made that the cross-sectional plane studied is representative of the entire volume underneath. Voigt average represents an upper bound for the overall modulus, and is calculated assuming that the strain is

ISBN: 978-988-14047-7-0
ISSN: 2078-0958 (Print); ISSN: 2078-0966 (Online)

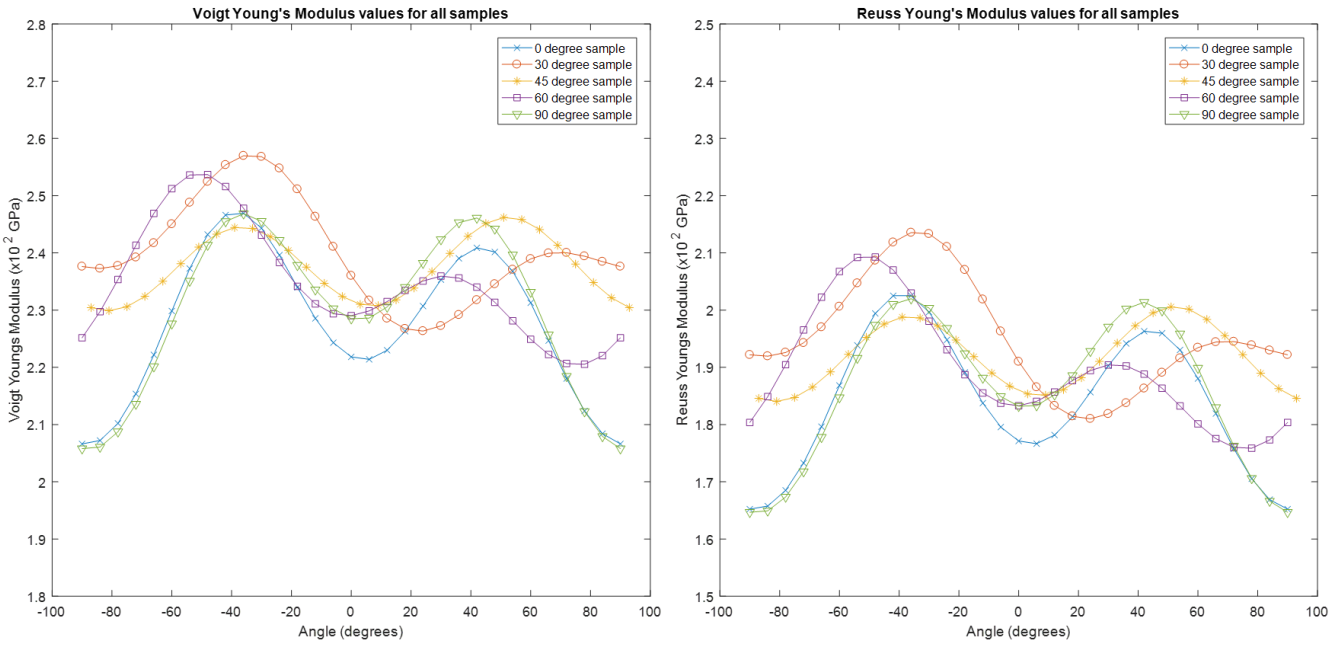

Figure 1: Voigt and Reuss Young's Modulus plots for each sample, taken over a range of angles from -90° to 90° in 6° intervals

everywhere uniform. In addition, a lower bound (Reuss average) is found assuming that the stress is everywhere uniform. The underlying models represent two different approaches to averaging, and are expressed by the following equations:

$$\hat{E} = \frac{\hat{\sigma}}{\hat{\varepsilon}} = \frac{\sum f_i(E_i\hat{\varepsilon})}{\hat{\varepsilon}} \quad \hat{E} = \sum f_i E_i \qquad \text{(Voigt)}$$

$$\hat{E} = \frac{\hat{\sigma}}{\hat{\varepsilon}} = \frac{\hat{\sigma}}{\sum f_i(\frac{\hat{\sigma}}{E_i})} \quad \frac{1}{\hat{E}} = \sum \frac{f_i}{E_i} \qquad \text{(Reuss)}$$

Young's modulus for each sample was computed at 15° intervals for the range of directions between -90° and 90° degrees angle with respect to *ND*, with the overall span of 180°. Figure 4 shows plots of the Voigt and Reuss averages for all five samples.

Table 3: Young's modulus peak amplitude angles

Sample	Peak 1	Peak 2
0°	42°	-39°
30°	69°	-36°
45°	51°	-39°
60°	33°	-51°
90°	42°	-36°

It can be observed that whilst Young's modulus curves for all samples have similar shapes, there are significant differences in the peak heights and positions. Table 3 shows the peak positions for all samples. The 0° and 90° samples have near identical peak positions, differing in their amplitudes by up to ~4%. In contrast, the 30°, 45° and 60° samples show significant differences in the amplitude. The maxima for the 30° sample lie at -36° and 69°, whereas the for the 60° sample they are found at -51° and 33°, respectively.

Despite the limited data extent and quality, the observed variation in the modulus appears to arise from the underlying difference in the sample ODF. We note that, in turn, the ODF is the consequence of the build sequence employed. Thus, we are able to conclude that judicious selection of the build orientation in additive manufacturing can be used to exercise control over the mechanical properties of the samples, without changing the stock powder material.

In fact, initial experimental investigations (tensile tests) on the family of dogbones prepared for the present study revealed measureable differences in the longitudinal stiffness between samples that are qualitatively consistent with the trends described above. This provides some confidence in the validity of the conclusions be drawn here on the basis of the crystal orientation analysis presented above.

C. Fourier Coefficients

In this section we pose further questions concerning the effect of the build direction on the orientation dependence of the sample stiffness. It is convenient to use global axes (*ND*, *RD* and *TD*) for this analysis. Indeed, if the orientational variation of stiffness only depends on the growth direction, then all plots in Figure 4 must come out similar. The fact that there are clear differences seen between the plots suggests that there are other effects present, i.e. the sample texture (and therefore the stiffness variation with the orientation) change as the consequence of the interaction between the build direction and sample axis orientation (and hence the geometry of the individual cross sections deposited in each layer). Since the differences in Young's modulus variation arise from the ODF, we need to seek further insight into the sample-to-sample differences in this parameter.

An ODF can be expressed in the form of a series of spherical harmonics:

$$f(g) = \sum_{l=0}^{\infty} \sum_{m=-l}^{+l} \sum_{n=-l}^{+l} C_l^{mn} T_l^{mn}(g)$$

where T_l^{mn} are the symmetric generalized spherical harmonic functions, and C_l^{mn} are the respective coefficients, g is the argument that represents crystal orientation. In terms of the Euler angles, this can be expressed as:

ISBN: 978-988-14047-7-0
ISSN: 2078-0958 (Print); ISSN: 2078-0966 (Online)

$$f(\phi 1, \Phi, \phi 2) = \sum_{l=0}^{\infty} \sum_{m=-l}^{+l} \sum_{n=-l}^{+l} C_l^{mn} e^{im\phi} P_l^{mn}(\Phi)$$

The coefficients C_l^{mn} can be found using the following relation:

$$C_l^{mn} = (2l+1) \oint f(g) T_l^{*mn}(g) dg$$

These are the Fourier coefficients which are plotted for each sample in Figure 5. Fourier coefficients are of particular importance for the calculation of mean macroscopic properties, e.g. second order coefficients are related closely to thermal expansion, electrical conductivity and the optical refraction index, whereas the fourth order coefficients are most closely linked to the elastic properties of the sample. It should be noted that the spatial variation of the elastic stiffness matrix must transform according to the fourth order polynomial of the rotation angle sine and cosine functions, whereas thermal conductivity and thermal expansion must follow a second order polynomial of the same kind.

Table 4: Fourth-order Fourier coefficients for all samples

Sample	Fourth-order Fourier coefficients
0°	0.5411
30°	0.3539
45°	0.09761
60°	0.2648
90°	0.5174

Table 5: Fitted polynomial coefficients

Coefficient	Fourth-order Fourier coefficients
P_1	0.5411
P_2	0.3539
P_3	0.09761

Table 6: Goodness of fit ($f(x) = p_1 x^2 + p_2 x + p_3$)

Coefficient	Value	95% confidence bound
P_1	0.0001612	-6.577×10^{-5}
P_2	-0.01504	-0.03662
P_3	0.5603	0.1047

Figure 5 illustrates the Fourier coefficients for different sample's ODF's, normalised in a consistent fashion so that the zero order term coefficient is equal to unity. It is clear that the meaningful difference between samples is found to be present in the fourth order Fourier coefficient. The values of these coefficients are given in Table 4. The 0° and 90° sample coefficients are very close (0.5411 and 0.5174 respectively), which is reflected in the similarity of the shapes and magnitudes of their Young's Modulus plots in Figure 3. The 30° sample and 60° sample have magnitudes of 0.3539 and 0.2648 respectively, whereas the 45° sample has a coefficient of 0.09761, considerably lower than any of the others.

Matlab was used to perform curve-fitting on the fourth order Fourier coefficient values; the fitted curve is shown in Figure 6. In the absence of points between 0° and 30°, or 60° and 90°, it is assumed that the fit can be described by a second order polynomial. The fitted equation coefficients are shown in Table 5, and the goodness of fit details are given in Table 6.

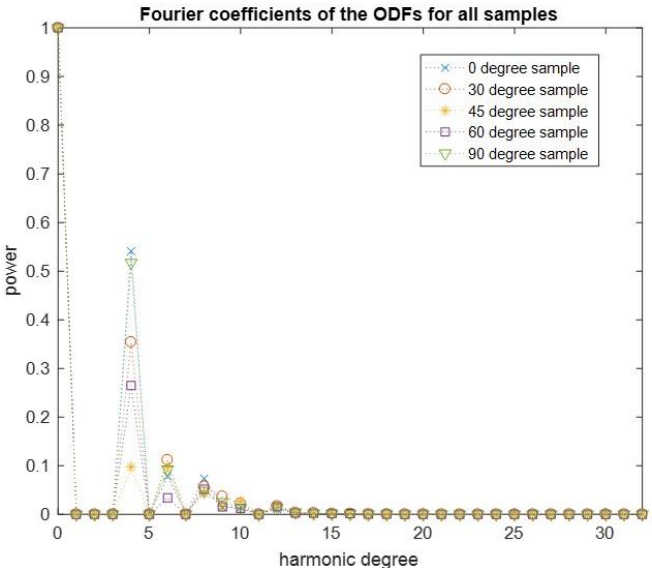

Figure 5: Fourier coefficients of each sample's orientation distribution function (ODF)

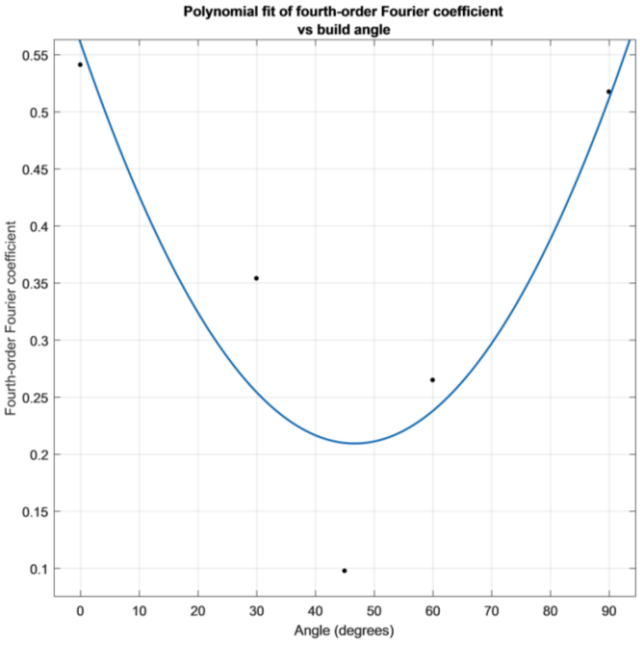

Figure 6: Fitted scatter plot of the fourth-order Fourier coefficients of each sample

IV. Conclusions

MTEX reconstruction of the sample ODF's based on EBSD mapping reveals that there are significant differences in the grain shape and orientation on different faces of the samples in the series studied here. EBSD data indicates predominant grain elongation and preferred orientation associated with the growth direction regardless of build orientation. This exerts notable effect on the sample stiffness in the longitudinal direction, with the maximum values of predicted moduli according to Voigt and Reuss found for the 45° sample. Nevertheless, we also note that the angle with respect to the growth direction alone is not sufficient to predict all sample properties.

The statistically significant differences in amplitude and shape of the Young's Modulus curves of different samples indicates that there must be significant variations in the ODF

ISBN: 978-988-14047-7-0
ISSN: 2078-0958 (Print); ISSN: 2078-0966 (Online)

of samples produced at different build angles that are not attributable to the approximations resulting from using EBSD data to calculate said ODFs. The curve fitting of the fourth-order Fourier coefficients of each ODF indicate that these variations can be roughly expressed by a constant ODF for all samples with a first order angle-dependent perturbation.

Further research should confirm the predictions made based on Young's modulus analysis by testing the response of all three samples when subject to loading along their respective longitudinal axes. Also, the effects of plastic flow on intergranular strains and stresses will be considered [3]. Powder diffraction using neutrons or X-rays would allow interrogating larger numbers of grains in the interior of the samples. This would enable more accurate reconstruction of the ODF for each sample, enabling a more precise calculation of samples' Young's moduli and ODF Fourier coefficients.

ACKNOWLEDGMENT

AMK acknowledges the support of EPSRC through grants EP/I020691 "Multi-disciplinary Centre for In-situ Processing Studies (CIPS)", EP/G004676 "Micromechanical Modelling and Experimentation", EP/H003215 "New Dimensions of Engineering Science at Large Facilities", and funding received for the MBLEM laboratory at Oxford through EU FP7 project iSTRESS (604646). Diamond Light Source is acknowledged for providing the beam time, and the Research Complex at Harwell for the provision of space and facilities.

Support from SIMTech is acknowledged through SIMT/14-230003, Selective Laser Melting (WP2), and SIMT/16-230001, Development of Hybrid 3D Additive + Subtractive Manufacturing Equipment (WP4).

REFERENCES

[1] F. Bachmann, R. Hielscher, H. Schaeben, Texture Analysis with MTEX - Free and Open Source Software Toolbox. Solid State Phenomena, 160, 63-68 (2010).

[2] E Salvati, T. Sui, A.M. Korsunsky, Uncertainty quantification of residual stress evaluation by the FIB–DIC ring-core method due to elastic anisotropy effects. Intl. J. Solids and Structures, 87, 61-69 (2016).

[3] A.M. Korsunsky, M.R. Daymond, K.E. James, The correlation between plastic strain and anisotropy strain in aluminium alloy polycrystals, Materials Science and Engineering A, 334, 41-48 (2002).

ISBN: 978-988-14047-7-0
ISSN: 2078-0958 (Print); ISSN: 2078-0966 (Online)